JOURNAL OF GLACIOLOGY

CAMBRIDGE UNIVERSITY PRESS

THIS MANUSCRIPT HAS BEEN SUBMITTED TO THE JOURNAL OF GLACIOLOGY AND HAS NOT BEEN PEER-REVIEWED.

Ice flow model emulator based on physics-informed deep learning

Journal:	*Journal of Glaciology*
Manuscript ID	Draft
Manuscript Type:	Article
Date Submitted by the Author:	n/a
Complete List of Authors:	Jouvet, Guillaume; University of Lausanne, Faculty of Geosciences Cordonnier, Guillaume; Université Côte d'Azur,
Keywords:	Glacier flow, Glacier modelling, Glacier mechanics, Ice-sheet modelling
Abstract:	Convolutional Neural Networks (CNN) trained from high-order ice flow model realizations have proven to be outstanding emulators in terms of computational-to-fidelity performance. However, the dependence on an ensemble of realizations of an instructor model renders this strategy difficult to generalize to a variety of glacier shapes and ice flow found in the nature. To overcome this issue, we adopt the approach of physics-informed deep learning, which fuses traditional numerical solving by finite differences/elements and deep learning approaches. Here, we train a CNN to minimise the energy associated with high-order ice flow equations either offline over a glacier catalogue or online directly within the time iterations of a glacier evolution model. As a result, our emulator is a promising alternative to traditional solvers thanks to its high computational efficiency (especially on GPU), its high fidelity to the

	original model, its simplified training (without requiring any data), its capability to handle various ice flow and memorize previous solutions, and its relative simple implementation. Embedded into the ``Instructed Glacier Model'' (IGM) framework, the potential of the emulator is illustrated with three applications including a large-scale high-resolution (2400x4000) forward glacier evolution model, an inverse modelling case for data assimilation, and an ice shelf.

Journal of Glaciology, Vol. 00, No. 0, 0000

Ice flow model emulator based on physics-informed deep learning

Guillaume Jouvet[1], Guillaume Cordonnier[2]

[1] *Université de Lausanne, IDYST, 1015 Lausanne, Switzerland*

<guillaume.jouvet@unil.ch>

[2] *Centre Inria de l'Université Côte d'Azur, Sophia-Antipolis, France*

ABSTRACT. Convolutional Neural Networks (CNN) trained from high-order ice flow model realizations have proven to be outstanding emulators in terms of computational-to-fidelity performance. However, the dependence on an ensemble of realizations of an instructor model renders this strategy difficult to generalize to a variety of glacier shapes and ice flow found in the nature. To overcome this issue, we adopt the approach of physics-informed deep learning, which fuses traditional numerical solving by finite differences/elements and deep learning approaches. Here, we train a CNN to minimise the energy associated with high-order ice flow equations either offline over a glacier catalogue or online directly within the time iterations of a glacier evolution model. As a result, our emulator is a promising alternative to traditional solvers thanks to its high computational efficiency (especially on GPU), its high fidelity to the original model, its simplified training (without requiring any data), its capability to handle various ice flow and memorize previous solutions, and its relative simple implementation. Embedded into the "Instructed Glacier Model" (IGM) framework, the potential of the emulator is illustrated with three applications including a large-scale high-resolution (2400x4000) forward glacier evolution model, an inverse modelling case for data assimilation, and an ice shelf.

INTRODUCTION

In glacier and ice sheet models, ice is commonly described as a viscous non-Newtonian [Glen, 1953] fluid whose motion is governed by the 3D nonlinear Glen-Stokes equations [Greve and Blatter, 2009]. Solving of these equations usually remain very costly compared to the modelling of other glacial underlying processes. To reduce the costs, the ice flow equations are often simplified by neglecting higher-order terms in the aspect ratio ϵ, which is usually small. The truncation of the second-order terms in ϵ yields the First-Order Approximation (FOA) model [Blatter, 1995], which consists of a 3D non-linear elliptic equation [Colinge and Rappaz, 1999] for the horizontal velocity and remains expensive. Going one step further, the Shallow Ice Approximation [Hutter, 1983] (SIA) is obtained after dropping the first-order terms in ϵ in the FOA model. As a result, the analytical solution of SIA is computationally inexpensive to implement. The SIA remains a reference model for many applications [e.g., Maussion et al., 2019], despite strongly-simplifying mechanical assumptions and applicability limited to areas where ice flow is dominated by vertical shearing [Greve and Blatter, 2009]. The transfer of numerical methods from Central Processing Units (CPU) on Graphics Processing Units (GPU) architectures is currently a promising approach to bypass the computational bottleneck associated with high-order modelling [Brædstrup et al., 2014], however, massive parallelisation of solvers on GPU remains a complex task [Räss et al., 2020].

As an alternative to solving directly ice flow physics, deep learning surrogate models (or emulators) have been found very promising in reduction of the solving costs with minor loss of accuracy [Brinkerhoff et al., 2021, Jouvet et al., 2022]. Deep learning is based on Artificial Neural Networks (ANNs), which are trained to capture the most essential relationship between the input and the output of an instructor model. The ANN is intended to be an efficient substitute for the original model within the range defined by the training dataset. Following this strategy, the computationally expensive Glen-Stokes model could be emulated by a simple Convolutional Neural Network (CNN) by Jouvet et al. [2022] with a speedup of several orders of magnitudes and high fidelity levels in the case of mountain glaciers, and major benefits for inverse modelling purposes [Jouvet, 2023]. Another key asset of ANNs is that they run very efficiently on GPUs, permitting additional significant speed-ups, especially when modelling high spatial resolution domains. However, the dependence on an instructor model makes the training of such an emulator technically difficult, not very flexible, and therefore limits its ability to generalize its validity range beyond the training data and its given spatial resolution.

In recent years, Physics-informed neural networks (PINNs) have emerged as a powerful approach in surrogate modelling to enforce directly physical laws (such as partial differential equations) in the learning process instead of matching datasets generated from physical models [e.g., Raissi et al., 2019]. Basic PINNs are trained to minimise the residual associated with the equations and the boundary conditions [Markidis, 2021]. In contrast, Variational PINNs (VPINNs) exploit the minimization form (or equivalently the variational form) of the problem as loss function [Kharazmi et al., 2019], which has the advantage of involving derivatives of lower orders compared to residuals. An important aspect of VPINNs is their connections with traditional Finite Element Methods (FEM). For example, a standard FEM solver applied to an elliptic problem represents the solution in a finite element approximation space spanned by mesh-defined basis functions and seeks the function that minimises the associated energy in the approximation space [Ern and Guermond, 2004]. On the contrary, the Deep-Ritz method proposed by Yu et al. [2018] (which belongs to the category of VPINN) represents the solution as a neural network in an approximation space generated by the parameters of a neural network.

In ice flow modelling, PINNs have been used by Riel et al. [2021] to learn the time evolution of drag in glacier beds from observations of ice velocity and elevation and by Riel and Minchew [2022] to calibrate ice flow law parameters and perform uncertainty quantification. Recently, Cui et al. [2022] proposed a mesh-free method to solve Glen-Stokes equations using an approach inspired by the Deep-Ritz method.

In this paper, we take over the CNN ice flow emulator introduced previously by Jouvet et al. [2022] and propose a new training strategy inspired by VPINN to remove the dependence on an instructor model and obtain a more generic emulator that is easier to implement and faster to train. For that purpose, we exploit the minimisation form associated with the FOA model. First, we present a numerical scheme suitable for GPUs to efficiently solve the physical FOA model based on optimisation techniques commonly utilised in machine learning (automatic differentiation and stochastic gradient optimisers). Second, we train our CNN ice flow emulator at minimising directly the energy instead of minimizing the misfit with solutions from an instructor model as done previously (Fig. 1). A similar approach was used by Cordonnier et al. [2023] for modelling terrain formation by glacial erosion. Their target was to generate realistic images in computer graphics, whereas we propose a thorough evaluation of the method and its potential for glaciological applications.

The outlines of this paper are: First, we introduce the physical ice flow FOA model and its minimisation formulation. Second, we describe the spatial discretization and the energy-based FOA solver. Then, we

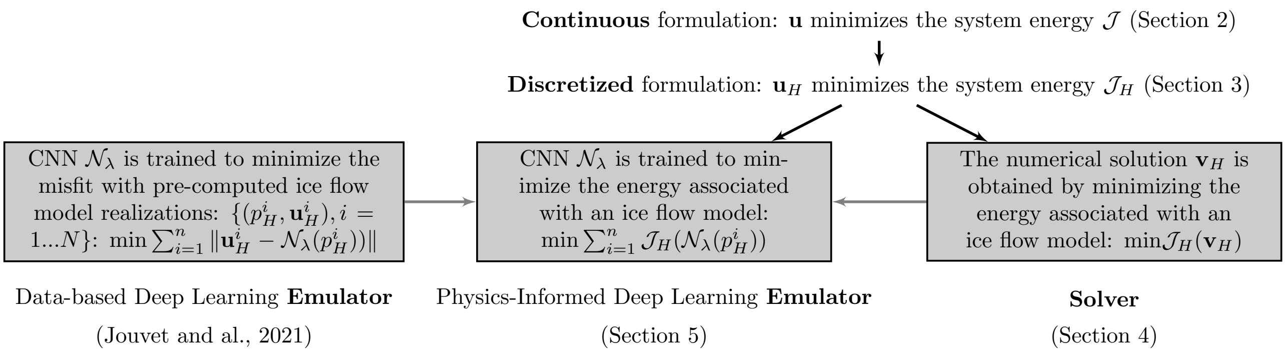

Fig. 1. Flowchart of the fusion of data-driven deep learning and traditional numerical solving strategies to design the Physics-Informed deep-learning emulator.

describe our deep learning emulator. and its implementation in the "Instructed Glacier Model" (IGM). Last, we present and discuss our assessment results, and examples of modelling applications.

MODEL

Let Ω be a rectangular horizontal domain supporting a glacier / volume of ice. Glacier bedrock and surface interfaces are defined by functions $b(x,y)$ and $s(x,y)$ where $(x,y) \in \Omega$. According to these definitions, the ice thickness h is defined as being the difference between the two: $h(x,y) = s(x,y) - b(x,y)$, and the three-dimensional volume of ice V is defined as

$$V = \{(x,y,z), b(x,y) \leq z \leq s(x,y), \quad (x,y) \in \Omega\},$$

which has two boundaries: the bedrock

$$\Gamma_b = \{(x,y,z), z = b(x,y), \quad (x,y) \in \Omega\}$$

and the surface

$$\Gamma_s = \{(x,y,z), z = s(x,y), \quad (x,y) \in \Omega\}$$

interfaces, see Figure 2. The two interfaces coincide in ice-free areas.

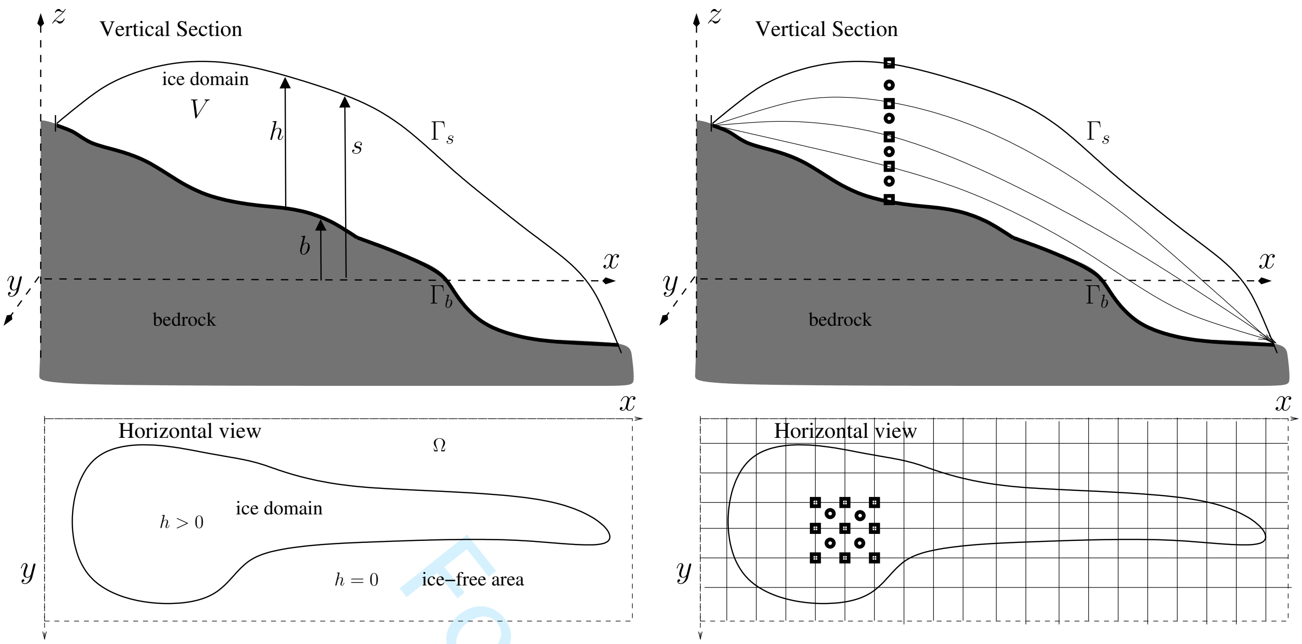

Fig. 2. Cross-section and horizontal view of a glacier with notations (left panel) and its spatial discretization (right panel), which is obtained using a regular horizontal grid and by subdividing the glacier into a pile of layers. All modelled variables (e.g. ice thickness) are computed at the corners of each cell of the 2D horizontal grid (materialised with squares) except the ice flow velocities, which are computed on the 3D corresponding grid. In contrast, the strain rate is computed on the staggered grid at the centre of each cells and layers (materialised with circles).

89 Glen-Stokes model

The Stokes model consists of the momentum conservation equation when inertial terms are ignored, together with the incompressibility condition:

$$-\nabla \cdot \sigma = \rho \mathbf{g}, \qquad \text{in } V, \tag{1}$$

$$\nabla \cdot \mathbf{u} = 0, \qquad \text{in } V, \tag{2}$$

where σ is the Cauchy stress tensor, $\mathbf{g} = (0, 0, -g)$, g is the gravitational constant and $\mathbf{u} = (u_x, u_y, u_z)$ is the 3D velocity field. Let τ be the deviatoric stress tensor defined by

$$\sigma = \tau - PI, \tag{3}$$

where I is the identity tensor, P is the pressure field, with the requirement that $\mathrm{tr}(\tau) = 0$ so that $P = -(1/3)\mathrm{tr}(\sigma)$. Glen's flow law [Glen, 1953], which describes the mechanical behaviour of ice, consists of the following nonlinear relation:

$$\tau = 2\mu D(\mathbf{u}), \tag{4}$$

where $D(\mathbf{u})$ denotes the strain rate tensor defined by

$$D(\mathbf{u}) = \frac{1}{2}(\nabla \mathbf{u} + \nabla \mathbf{u}^T), \tag{5}$$

μ is the viscosity defined by

$$\mu = \frac{1}{2} A^{-\frac{1}{n}} |D(\mathbf{u})|^{\frac{1}{n}-1}, \tag{6}$$

where $|Y| := \sqrt{(Y : Y)/2}$ denotes the norm associated with the scalar product (:) (the sum of the element-wise product), $A = A(x, y) > 0$ is the Arrhenius factor and $n > 1$ is the Glen's exponent. Note that A depend on the temperature of the ice [Paterson, 1994]. For simplicity, this paper assumes vertically constant ice temperature, however, this assumption can be released without further difficulties.

Boundary conditions

The boundary conditions that supplement (1), (2) are the following. No force applies to the ice-air interface,

$$\sigma \cdot \mathbf{n} = 0, \quad P = 0, \qquad \text{on } \Gamma_s, \tag{7}$$

where $\mathbf{n}$ is an outer normal vector along Γ_s. Along the lower surface interface, the nonlinear Weertman friction condition reads [Hutter, 1983, Schoof and Hewitt, 2013]

$$\mathbf{u} \cdot \mathbf{n} = 0, \tag{8}$$

$$[(I - \mathbf{n}\mathbf{n}^T)\tau] \cdot \mathbf{n} = -c^{-m} |(I - \mathbf{n}\mathbf{n}^T) \cdot \mathbf{u}|^{m-1} (I - \mathbf{n}\mathbf{n}^T) \cdot \mathbf{u}, \tag{9}$$

on Γ_b for $k \in \{x, y\}$, where $m > 0$, $c = c(x, y) > 0$, and $\mathbf{n}$ is the outward normal unit vector to Γ_b. The relation (9) relates the basal shear stress $[(I - \mathbf{n}\mathbf{n}^T)\tau] \cdot \mathbf{n}$ to the sliding velocity $(I - \mathbf{n}\mathbf{n}^T) \cdot \mathbf{u}$, both of them projected onto the tangential plane. Note that $c = 0$ in case of no-sliding.

Minimization formulation

The abovementioned Glen-Stokes problem can be reformulated into variational and minimisation problems. We follow the derivation made by Jouvet [2016]. For that, we consider the following divergence-free velocity space [Girault and Raviart, 1986]:

$$\mathcal{X} := \{\mathbf{v} \in [W^{1,1+\frac{1}{n}}(V)]^3, \quad \nabla \cdot \mathbf{v} = 0, \quad \mathbf{v} \cdot \mathbf{n} = 0 \text{ on } \Gamma_b\},$$

where $W^{1,p}$ is the appropriate Sobolev space [Adams and Fournier, 2003]. The variational formulation associated with the Glen-Stokes problem writes: Find $\mathbf{u} \in \mathcal{X}$ such that for all $\mathbf{v} \in \mathcal{X}$ we have:

$$\int_V A^{-\frac{1}{n}} |D(\mathbf{u})|^{\frac{1}{n}-1} (D(\mathbf{u}), D(\mathbf{v})) dV \tag{10}$$

$$+ \int_{\Gamma_b} c^{-m} |\mathbf{u}|_M^{m-1} (\mathbf{u}, \mathbf{v})_M dS + \rho g \int_V (\nabla s \cdot \mathbf{v}) dV = 0, \tag{11}$$

where the bilinear form $(\mathbf{a}, \mathbf{b})_M := (M\mathbf{a}) \cdot \mathbf{b}$, and its associated norm $|\mathbf{a}|_M := \sqrt{(\mathbf{a}, \mathbf{a})_M}$ have for matrix

$$M = \begin{pmatrix} I + (\nabla_{\mathbf{x}} b)(\nabla_{\mathbf{x}} b)^T & \mathbf{0} \\ \mathbf{0} & 0 \end{pmatrix}. \tag{12}$$

The above problem is equivalent to seeking for $\mathbf{u} \in \mathcal{X}$ such that

$$\mathcal{J}(\mathbf{u}) = \min\{\mathcal{J}(\mathbf{v}), \mathbf{v} \in \mathcal{X}\}, \tag{13}$$

where the functional to be minimised is

$$\mathcal{J}(\mathbf{v}) = \int_V 2 \frac{A^{-\frac{1}{n}}}{1+\frac{1}{n}} |D(\mathbf{v})|^{1+\frac{1}{n}} dV + \int_{\Gamma_b} \frac{c^{-m}}{1+m} |\mathbf{v}|_M^{1+m} dS$$
$$+ \rho g \int_V (\nabla s \cdot \mathbf{v}) dV. \tag{14}$$

It must be stressed that only the first term still depends on the vertical velocity in both formulations (11) and (14).

First-Order Approximation (FOA)

If one introduces the aspect ratio $\epsilon = [h]/[\mathbf{x}]$ of the ice geometry V, where $[h]$ and $[\mathbf{x}]$ denote its typical height and length. It is easy to verify that in that the strain rate tensor $D(\mathbf{v})$ contains terms scaling with ϵ^{-1}, ϵ^0, and ϵ^1. As glaciers are usually thin objects with a small aspect ratio ϵ, it is a common practise to omit the highest order term. By doing so and invoking the incompressibility equation, the vertical velocity components ($\partial_x u_z$ and $\partial_y u_z$) of the strain rate tensor can be eliminated:

$$D(\mathbf{u}) = \left(\begin{array}{ccc} \partial_x u_x & \frac{1}{2}\left(\partial_y u_x + \partial_x u_y\right), & \frac{1}{2}\left(\partial_z u_x\right) \\ \frac{1}{2}\left(\partial_y u_x + \partial_x u_y\right) & \partial_y u_y & \frac{1}{2}\left(\partial_z u_y\right) \\ \frac{1}{2}\left(\partial_z u_x\right) & \frac{1}{2}\left(\partial_z u_y\right) & -\partial_x u_x - \partial_y u_y \end{array} \right). \qquad (15)$$

In turn, this eliminates the vertical velocity component u_z from the ice flow model. The resulting model (so-called First-Order Approximation, FOA, or Blatter-Pattyn model [Blatter, 1995]) is obtained by minimising the functional $\mathcal{J}$ defined in (14) with $D(\mathbf{u})$ defined by (15). Advantageously, the constraints of the functional space $\mathcal{X}$ disappear when removing the vertical component of the velocity. As a result, the FOA model consists of a three-dimensional, non-linear, elliptic, and unconstrained problem, which is therefore simpler than the original Glen-Stokes problem. Provided suitable assumptions, one can show [Colinge and Rappaz, 1999] that the functional $\mathcal{J}$ is continuous, strictly convex and coercive in the functional space $[W^{1,1+\frac{1}{n}}(V)]^2$, therefore, the FOA problem admits a unique solution.

SPATIAL DISCRETIZATION

First, the horizontal rectangular domain Ω is discretised with a regular grid of size $N_x \times N_y$ with constant cell spacing H in the x and y direction (Fig. 2, right panel). Variables such as the ice thickness h, the surface topography s, the rate factor A, and the sliding coefficient c are defined at the corners of each grid cell of the horizontal grid. In the following, we use subscript H to denote these discrete quantities such as $\mathbf{u}_H$, h_H, s_H, A_H, c_H defined on the horizontal grid.

On the other hand, the ice thickness is discretised vertically using a fixed number of points N_z. Layers are distributed according to a quadratic rule such that discretisation is fine close to the ice-bedrock interface (where the strongest gradients are expected) and coarse close to the ice-surface interface following the strategy given by Bueler and Brown [PISM, 2009]. Subsequently, the approximation space X_H for velocities consists of piecewise linear functions defined at the corners of each grid cell in the horizontal direction and at the intersection of each layer in the vertical discretisation.

In finite elements, solving the nonlinear elliptic FOA problem occurs to minimise the associated functional $\mathcal{J}$ in a finite-dimension approximation space X_H spanned by shape functions defined in the discretised domain instead of the full continuous solution space X. We follow a similar strategy here: Given $p_H = (h_H, s_H, A_H, c_H)$, we seek for $\mathbf{u}_H \in X_H$ such that

$$\mathbf{u}_H = \text{argmin}\{\mathcal{J}_{p_H}(\mathbf{v}_H), \mathbf{v}_H \in X_H\} \tag{16}$$

where

$$\begin{aligned}\mathcal{J}_{p_H}(\mathbf{v}_H) = \int_\Omega \Bigg(& \frac{2A_H^{-\frac{1}{n}}}{1+\frac{1}{n}} \int_{s_H-h_H}^{s_H} |D_H(\mathbf{v}_H)|^{1+\frac{1}{n}} dz \\ & + \frac{c_H^{-m}}{1+m} |\mathbf{v}_H|_M^{1+m} dS \\ & + \rho g \int_{s_H-h_H}^{s_H} (\nabla s_H \cdot \mathbf{v}_H) dz \Bigg) d\Omega. \end{aligned} \tag{17}$$

For simplicity, D is approximated by a finite difference scheme on a 3D staggered grid (Fig. 2, right panel). As D involves derivatives in the three dimensions, we apply either a finite difference or cell averaging to ensure that all derivatives in (15) are approximated consistently on the same 3d staggered grid (i.e., at the centre of cells horizontally and at the middle of layers vertically). The two other terms (sliding and gravity force related) are also computed on the staggered grid (otherwise, this would cause numerical artefacts, typically chessboard modes). Due to the layer-wise vertical discretisation, we first compute the horizontal derivatives of D_H in a layer-dependent system of coordinate $(x, y, \tilde{z})$ where $\tilde{z} = z - l$ and l is the layer elevation, and transfer them in the reference system of coordinate (x, y, z) using a simple rule of derivative: e.g., $\frac{\partial f}{\partial x} = \frac{\partial \tilde{f}}{\partial x} - \frac{\partial \tilde{f}}{\partial z}\frac{\partial l}{\partial x}$ for any quantity f (resp. $\tilde{f}$) defined in (x, y, z) (resp. $(x, y, \tilde{z})$). Note that ice margins must be treated carefully to prevent singular vertical derivatives of D_H as the vertical step size tends to zero. To overcome this issue, we assume a minimum ice thickness of one metre.

SOLVER

The convex optimisation problem (16) is solved using the Adam optimiser [Kingma and Ba, 2014], which belongs to stochastic gradient descent methods, which are efficient on GPU. Using the Keras [Chollet et al., 2015] and Tensorflow [Abadi et al., 2015] libraries, the derivatives of $\mathcal{J}_{p_H}$ with respect to $\mathbf{v}_H$ are obtained by automatic differentiation. The optimisation scheme is initialised with zero ice velocity and stops at convergence. When used in transient glacier evolution runs, the gradient scheme uses the ice flow from the previous time step as initialisation to predict the next one. In the following, we refer to the "solved" solution (in contrast to the "emulated" solution), the result of the solver at convergence.

EMULATOR

We now set up an ice flow emulator, which predicts horizontal ice flow $(\mathbf{u}_H, \mathbf{v}_H)$ from the input field p_H, which includes ice thickness h_H, surface topography s_H, ice flow parameters A_H and sliding coefficient c_H, and spatial grid resolution H_H:

$$\begin{aligned} \mathcal{N}_\lambda : \quad \{h_H, s_H, A_H, c_H, H_H\} &\longrightarrow \{\mathbf{u}_H, \mathbf{v}_H\} \\ \mathbb{R}^{N_X \times N_Y \times 5} &\longrightarrow \mathbb{R}^{N_X \times N_Y \times N_Z \times 2} \end{aligned} \tag{18}$$

where input and output can be seen as two- and three-dimensional multichannel fields, which are defined on the regular horizontal grid (Fig. 3). Having these selected input parameters permits to develop a generic ice flow emulator that can handle a large variety of glacier shapes, types of ice flow (from shearing to sliding dominant), and spatial resolutions.

As an emulator, we choose an Artificial Neural Network (ANN), which maps input to output variables by a sequential composition of linear and nonlinear functions (or a sequence of network layers). Linear operations have weights $\lambda = \{\lambda_i, i = 1, ..., N\}$, which are optimised in the training stage. Here, we use a Convolutional Neural Network [CNN; Long et al., 2015], which is a special type of ANN that additionally includes local convolution operations to learn spatially variable relationships [LeCun et al., 2015]. Indeed, 2D CNNs proved to be capable of learning high-order ice flow models [Jouvet et al., 2022]. Here we retain the hyper-parameters found by Jouvet et al. [2022] as close to optimal in terms of model fidelity to computational performance (or model parameters). As a result, our CNN consists of 16 two-dimensional

[!ht]

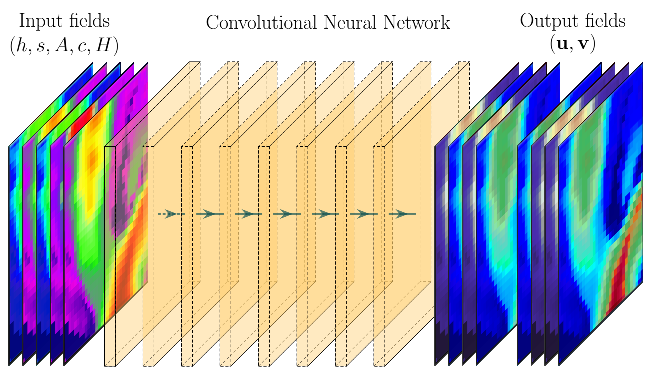

Fig. 3. Our emulator consists of a CNN that maps geometrical (thickness and surface topography), ice flow parameters (shearing and basal sliding), and spatial resolution inputs to 3D ice flow fields.

157 convolutional layers between input and output data (Fig. 3). Convolutional operations have a kernel 158 matrix (or feature map) of size 3×3. A padding is used to conserve the frame size through the convolution 159 operation. Convolutional operations are repeated using a sliding window with one stride across the input 160 frame and 32 feature maps. As a non-linear activation function, we use leaky Rectified Linear Units [Maas 161 et al., 2013]. As a result, our CNN has about 140'000 trainable parameters.

We differ from traditional Physics-Informed Neural Networks (PINNs) in two ways: first PINNs usually map the coordinate of the sampling points to the physical output, which forces them to retrain the network for different settings, while our inputs are essential model parameters. Second, PINNs usually minimise the residual of the equation and/or boundary conditions involved in the physical model [e.g., Markidis, 2021]. Instead, we adopt the different variational PINN strategy [Kharazmi et al., 2019] by minimising the energy associated with the FOA model instead of the residual (Fig. 1). In more detail, the training consists of finding the weights of CNN $\{\lambda_i, i = 1, ..., N\}$ that minimise the energy associated with FOA over an ensemble of inputs $\{p_H^i, i = 1, ..., n\}$:

$$\lambda = \text{argmin} \left(\sum_{i=1}^{n} \mathcal{J}_H(\mathcal{N}_\lambda(p_H^i)) \right). \tag{19}$$

162 The optimisation problem (19) is solved again using the Adam optimiser [Kingma and Ba, 2014], with 163 adaptive learning including an exponential decay to launch the training aggressively for efficiency and to 164 end it gently for fine-tuning. We additionally implement a learning-rate reinitialisation strategy to prevent 165 falling in local minima. In practise, our learning rate varies between 10^{-4} at initialisation and 10^{-6}. At

first view, the minimisation problem (19) is expected to be more difficult to solve than the (16) one, as there is no guarantee that $\mathcal{J}_H$ is convex with respect to the training parameters λ. On the other hand, problem (19) is expected to have much fewer control parameters (the number of training parameters is on the order of 10^5) than problem (16), which may have about 10^8 control parameters ($2 \times N_z \times N_y \times N_x$) when treating a large scale array.

Later we explore two training strategies: i) an offline training (or pre-training) that consists of training our CNN by sampling glaciers from an existing glacier shape catalogue (Appendix A), and parameters randomly ii) an online training (or re-training) performed within the time loop of transient glacier evolution model runs. In offline training, one optimises using batches (a batch size of 8 was used here) to facilitate convergence, while only a single glacier sample could be used for online training at each iteration ($n = 1$ in (19)). In both cases, the solutions obtained from the pre/retrained emulator are referred to as "emulated" in the following (in contrast to the "solved" one seen in the previous section).

IMPLEMENTATION IN THE GLACIER EVOLUTION MODEL IGM

Both the solver and emulator are implemented in the "Instructed Glacier Model" (IGM, `https://github.com/jouvetg/igm`), which couples ice dynamics and Surface Mass Balance (SMB) through mass conservation to simulate glacier time evolution given an initial glacier geometry and climate or SMB forcing [Jouvet et al., 2022]. IGM code relies on operations of the TensorFlow library to allow vectorial/parallel operations between large arrays that are computationally efficient on GPU. Conveniently, IGM deals with data defined on a given 2D raster regular grid consistently with spatial discretisation (Fig. 2). The workflow/structure of an IGM-based glacier evolution Python code is given in Fig. 4, and described step-by-step in the following paragraph.

First, the Tensorflow library and the class `Igm` are loaded from the IGM code. Then, an object `glacier` of the class is defined. `Igm`, which contains both variables (e.g., thk for distributed ice thickness, smb for the distributed surface mass balance) and functions to run a glacier evolution simulation. Then, the parameters may be changed prior to the call of `glacier.initialize()`. After setting the computation either on GPU or CPU, the input distributed data is read from a NetCDF file with `glacier.load_ncdf_data()`, and all other fields are initialised with `glacier.initialize_fields()`. Finally, the time loop includes a series of steps. First, the SMB is computed from a given (IGM includes simple parameterisations based on ELA and a climate-driven PDD model) or user-defined IGM function. Then the ice flow is computed from the emulator in `glacier.update_iceflow_emulated()`. Prior to this step, an online retraining of the emulator at a given frequency can be ordered with command `glacier.update_iceflow_emulator()`. Then, the time step is computed adaptively in `update_t_dt()` to satisfy the CFL condition:

$$\Delta t = \min\{CH/\|\bar{\mathbf{u}}\|_{L^\infty}, \Delta t_{min}\} \tag{20}$$

where $C < 1$, $\bar{\mathbf{u}}$ is the vertically average horizontal ice flow velocities, and H is the grid cell spacing. Last, the ice thickness is updated by solving one step of the mass conservation equation using a first-order upwind finite-volume scheme in `glacier.update_thk()`. The rest of the function permits to write output model information through the iterations. Anytime in the loop, one can access or modify any field variables, e.g., the ice thickness with `glacier.thk`.

Note that it is easy to switch from the "emulated" to the "solved" solution in the sketch of code given in Fig. 4, replacing `glacier.update_iceflow_emulated()` by function `glacier.update_ice-flow_solved()`, however, making sure that the configuration parameters controlling the number of solving iterations and/or the time step Δt_{min} are adjusted.

RESULTS

In this section, we present in turn i) comparisons between reference and "solved" solutions for the ISMIP-HOM experiments [Pattyn and others, 2008] in order to test the solver and its implementation, ii) comparisons between "solved" and "emulated" ice flow solutions for a test glacier after offline training on the glacier catalogue, iii) comparisons between "solved" and "emulated" solutions within time evolution simulations with and without online retraining of the emulator, iv) computational performance of each method.

ISMIP-HOM validation solutions

ISMIP-HOM [Pattyn and others, 2008] experiments consist of modelling exercises based on various synthetic ice geometries and boundary conditions to produce different types of ice flow, which can be met in real glacier modelling. Here, we focus on ISMIP-HOM experiments A and C, which represent a wide panel of various 3D ice flow (from shearing to sliding-dominant flows) over a squared horizontal domain of length

[!ht]

```
import tensorflow as tf
from igm import Igm

# Define an object of class Igm
glacier = Igm()

# Change parameters
glacier.config.tstart = 2000
glacier.config.tend   = 2200
glacier.initialize()

# Set the computation on GPU or CPU
with tf.device("/GPU:0"):

  # Read input raster data
  glacier.load_ncdf_data()
  glacier.initialize_fields()

  # Time loop
  while glacier.t < glacier.config.tend:
    glacier.update_smb()
    glacier.update_iceflow_emulator()
    glacier.update_iceflow_emulated()
    glacier.update_t_dt()
    glacier.update_thk()
    glacier.update_ncdf_ex()
```

Fig. 4. IGM structure of the code for forward glacier evolution model.

$L > 0$: $\Omega = [0, L] \times [0, L]$. In experiment A, the ice geometry is defined by

$$s(x, y) = -x \tan(0.5°),$$
$$b(x, y) = s(x) - 1000 + 500 \sin(2\pi x/L) \sin(2\pi y/L),$$

and a no-slip condition is prescribed on the bedrock, while, in experiment C, the geometry is defined by

$$s(x, y) = -x \tan(0.1°),$$
$$b(x, y) = s(x, y) - 1000,$$

and a slip condition is prescribed everywhere on the bedrock defined by $m = 1$ and

$$c(x, y) = [1000 \times (1 + \sin(2\pi x/L) \sin(2\pi y/L))]^{-1}.$$

In both experiments, we use $A = 100$ MPa^{-3} a^{-1} as Arrhenius factor in Glen flow law, and horizontal periodic boundary conditions connect the four horizontal sides of Ω, see Pattyn and others [2008] for further details. The squared horizontal domain Ω was divided into 100 cells in both horizontal directions to generate a regular grid, while the ice thickness is divided into 20 layers. To obtain a wide range of aspect ratios, we performed both experiments for several values of domain length L = 10, 20, 40, 80, and 160 km. Figure 5 compares the "solved" solutions with the reference 'oga1' solution obtained from Pattyn and others [2008] for all experiments.

As a result, we generally find a very good agreement between the two solutions. In line with model intercomparisons [Pattyn and others, 2008], there are small discrepancies in the experiments that have the smallest domain length L, which are known to be more sensitive to numerical parameters and schemes. This validates our numerical solver and verifies that the system energy (17) – which is used for solving and training the CNN – is correctly implemented.

Stationary solutions with offline training

Here we exploit the glacier catalogue presented in Appendix A (Fig. 17) in order to test i) the solver and ii) the emulator with a test glacier shape, and assess the accuracy of the "emulated" solution with respect to the "solved" one. First, we fix the ice flow parameters (A, c) and the spatial resolution H to constant

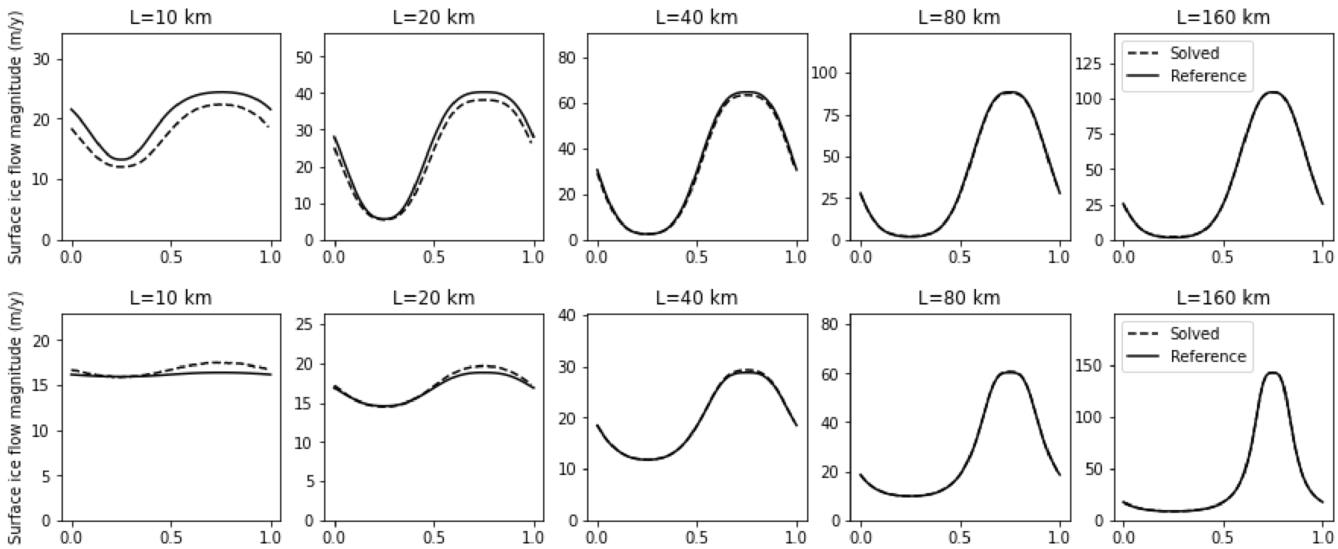

Fig. 5. Surface ice flow magnitude along the $y = L/4$ horizontal line for different length scales L = 10, 20, 40, 80, and 160 km in the ISMIP-HOM experiments A and C: comparison between "solved" with reference solution 'oga1' obtained from Pattyn and others [2008]. For simplicity, the x-axis was scaled with L.

standard values ($A = 78$ MPa^{-3} a^{-1}, $c = 10$ km MPa^{-3}, $H = 100$ m) for simplicity. In a second time, we will vary these parameters at training.

A test glacier is selected in addition to the glacier catalogue, and a "solved" ice flow solution is obtained for this glacier by minimising the associated energy with the Adam optimiser. Figure 6 presents the results in terms of input data (panels A and B), "solved" solution (panel C), and decrease in system energy (panel D). As a result, the Adam optimiser is efficient at minimising the energy and capturing the solution, whose convergence is reached after about 1000 iterations. Smooth convergence is attributed to the convexity of $\mathcal{J}$ with respect to $\mathbf{u}$ [Jouvet, 2016], and the choice of an appropriate step size.

Aside from the solver, we have trained a CNN emulator over the glacier catalogue (so that the CNN meets a large ensemble of realistic inputs, Fig. 17) to minimise the system energy (solving the optimisation problem (19)), and evaluated its performance to reproduce the previously "solved" solution on a test glacier. Figure 7 presents the results in terms of "emulated" solution when the training has converged (panel A), the difference between "solved" and "emulated" solutions (panel B), and the decrease in the system energy through training iterations (panel D). The fidelity of the "emulated" solution $\mathbf{u}_E$ towards the "solved" solution $\mathbf{u}_S$ is measured by taking the relative norm L_1 between the two:

$$E_{L_1} = \frac{\|\mathbf{u}_E - \mathbf{u}_S\|_{L^1}}{\|\mathbf{u}_S\|_{L^1}}, \text{ where } \quad \|\mathbf{u}\|_{L^1} = \int_\Omega \int_b^{b+h} |\mathbf{u}|_1. \tag{21}$$

[!ht]

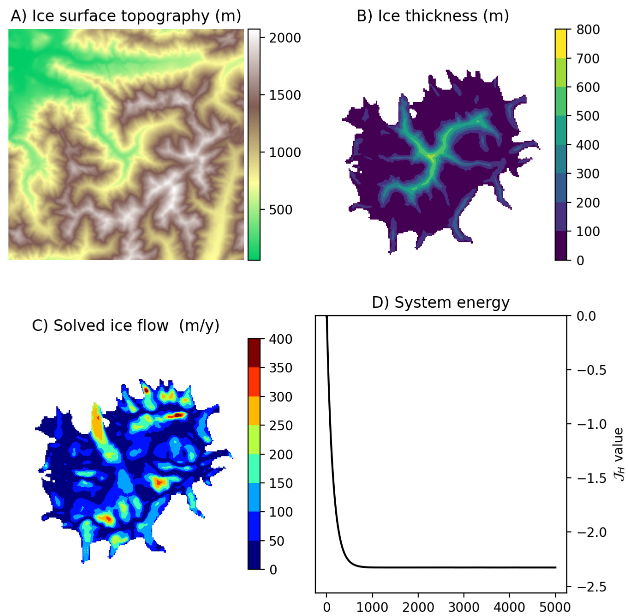

Fig. 6. Results of the solver on the "test" glacier: A) Ice surface topography and B) ice thickness of the "test" glacier C) "solved" surface ice flow solution at convergence D) evolution of the system energy through the iterations of the Adam optimiser.

The evolution of the relative norm L_1 (panel C, Fig. 7) shows that the emulator captures well the ice flow after about 3000 iterations (the L1 relative error drops to 10-15%). The effect of the adaptive learning rate (initially fixed at 10^{-4}, with exponential decay) is clearly visible: The first stage of training (iterations 0 to 1000) shows the largest decays and oscillations, while the last stage (iterations 4000 to 5000) is characterised by a smoother but slower decay. Interestingly, the energy associated with the "emulated" solution decreases towards a value ($\sim$ -2.2) that is relatively close to the value obtained when solving ($\sim$ -2.3), demonstrating that our CNN has learnt well to minimise the energy. Although the "emulated" and "solved" solutions show a high degree of similarity (compare panel C of Fig. 6 with panel A of Fig. 7), the spatial pattern of the difference between the two (Fig. 7, panel B) reveals that the error is unevenly distributed, the highest discrepancy being found on the most prominent glacier tongue. This is presumably due to the relatively poor representation of large, fast-flowing glacier tongues in the glacier catalogue compared to a smaller one [Jouvet et al., 2022].

In a second time, we take over the emulator trained with fixed values of A, c, and H, and continue training with varying values (but spatially constant) $A \in [20, 100]$ MPa^{-3} a^{-1}, $c \in [0, 20]$ km MPa^{-3} a^{-1}, and $H = 100, 200$ m. The ice flow parameters (A, c) were sampled with a uniform distribution within

[!ht]

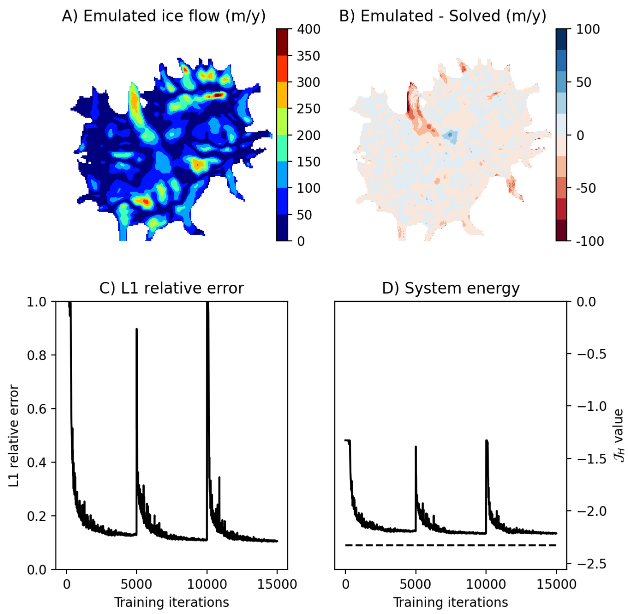

Fig. 7. Results of the emulator on the "test" glacier: A) "Emulated" surface ice flow at the surface of the test glacier (Fig. 6) at convergence of the offline training over the catalogue, B) difference between the "emulated" and "solved" solutions C) evolution of the L1 relative error between the two solutions and D) of the system energy through the training epochs.

their ranges, while the spatial resolution H_H (initially 100 m) was randomly changed to 200 m by simple data upscaling. As a result, the CNN meets a large set of input parameters in terms of glacier shape (sampling into the catalogue as before) and other parameters. To assess the performance of the emulator, we compare "emulated" and "solved" solutions obtained with 5 sets of parameters (A, c, H) for the test glacier in Figure 8. As a result, the emulator generally captures well the ice flow for various parameter sets (compare the first and second rows of Figure 8). However, we find relatively high spatial discrepancies when displaying the difference between the two (third row of Figure 8), with L1 relative values up to 20% (and 30% when using a different A, last row of Figure 8). Such a deteriorated accuracy is not surprising: the storage capacity of our CNN model emulator has reached its limit, and one cannot expect a model of a given size (about 140000 parameters) to store more realisations with a similar accuracy.

The storage limitation motivates a custom training (or the online retraining strategy used in the next section): we continue the training with a set of variable parameters (A, c, H), but using the sole glacier test shape (which was ignored in the initial training) and fixed parameters instead of the glacier catalogue. The goal of this last experiment is to assess the added value of an emulator customised for specific glacier

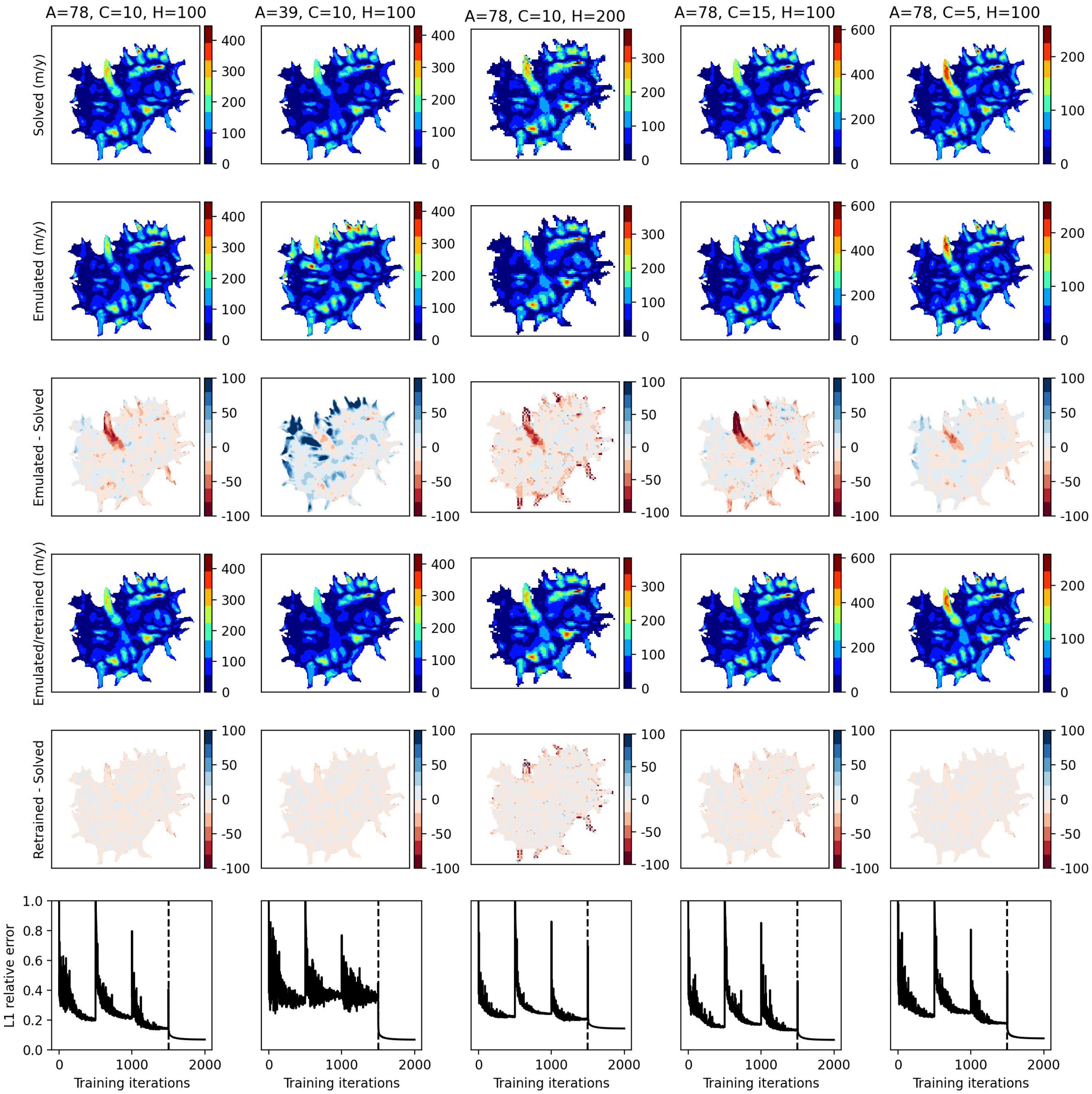

Fig. 8. Results of the emulator on the "test" glacier with varying values of A, c, and H. Each column corresponds to one parameter set (A, c, H) (the first column shows the default original parameters). The first row displays the "solved" surface ice flow solution. The second (resp. fourth) row displays the "emulated" solution after training over the glacier catalogue (resp. the single test glacier shape), while the third (resp. fifth) shows the difference between this solution and the "solved" one. The last raw shows the L1 relative error through the training (first 15000 iterations using the glacier catalogue, last 5000 iterations using the test glacier shape only, the two being separated by the vertical dashed line).

shapes and parameters (i.e., compared to a more generic emulator trained using a larger ensemble of glacier settings). Therefore, training the emulator only on the test glacier shape and parameters permits to significantly reduce the discrepancy in spatial pattern (compare the third and fifth rows of Figure 8) and to reduce the L1 relative error below 10%.

Transient solutions with online training

We now conduct experiments on transient glacier evolution of real-world glaciers to assess the performance and accuracy of our emulator (w.r.t. the solver) in modelling applications. We consider two glaciers of different sizes i) the present-day Aletsch Glacier, Switzerland, which is the current largest glacier of the European Alps [Jouvet and Huss, 2019] ii) the former Valais Glacier, Switzerland, which covered a large part of Switzerland during the last glacial maximum [Jouvet et al., 2017]. The experiments for these two glaciers cover different applications, from individual glaciers on a small grid (244x179 at 100 m resolution for Aletsch) relevant for the modelling of today's glaciers to ice fields on a large grid (700x700 at 200 m resolution for Valais) relevant for paleo glacier modelling.

For each glacier, we perform two kinds of experiments: i) the first (referred to as "ELA-varying") assumes fixed ice flow parameters (A and c), and forces the Surface Mass Balance (SMB) with time-varying Equilibrium Line Altitudes (ELA) ii) ; the second (referred as "A/c-varying") assumes fixed ELA and force time-varying ice flow parameters (A and c). As SMB, we use a simple parameterisation based on given ELA z_{ELA}, vertical gradients of accumulation and ablation, and maximum accumulation rate:

$$SMB(z) = \begin{cases} \min(0.003 \times (z - z_{ELA}), 1), & \text{if } z \geq z_{ELA} \\ 0.006 \times (z - z_{ELA}), & \text{otherwise.} \end{cases}$$

Prior to running experiments, we collected the bedrock topography of the two regions [Grab, 2020], initialised the model with ice-free conditions and ran it with ice flow parameters $c = 10$ km MPa^{-3} a^{-1} and $A = 78$ MPa^{-3} a^{-1} and mass balance parameters $z_{ELA} = 2800$ m asl, and $z_{ELA} = 2200$ m asl for Aletsch and Valais, respectively. The goal of this preliminary phase is to simulate the build-up of glaciers until they reach a steady state shape. Then, the ELA-varying transient experiment consists of modelling 2000 years (starting from the obtained steady-state shape, and keeping the parameters constant) with the following

ELA parametrisation:

$$z_{ELA} = 2800 + 200 \times \sin(\pi t/500) \text{ m},$$
$$z_{ELA} = 2200 + 300 \times \sin(\pi t/500) \text{ m},$$

for the Aletsch and Valais glaciers, respectively. On the other hand, the A/c-varying transient experiment consists of running the model for 2000 years (starting from the obtained steady-state shape and keeping the parameters constant) with the following ice flow parameters:

$$A = 78 + 22 \times \sin(\pi t/500) \text{ MPa}^{-3}\text{a}^{-1},$$
$$c = 10 + 5 \times \sin(\pi t/500) \text{ km MPa}^{-3}\text{a}^{-1},$$

to induce glacier variations (retreat-advance-retreat), and explore a variety of configurations for assessment.

The experiments were performed using different strategies to compute the ice dynamics; i) using the solver (this is our reference run) ii) using the emulator trained (offline) in the previous section from the glacier catalogue iii) using the emulator with adaptive online retraining over the first 1000 years and releasing the retraining for the last 1000 years iv) using adaptive online retraining as before, but keeping a light 10% retraining over the last 1000 years (once every 10 iterations) instead of cancelling completely. The last setting aims to investigate the memory of the emulator. Figures 9, 10, 11, and 12 show the results of the ELA and A/c-varying experiments for Aletsch and Valais Glacier, respectively, in terms of fidelity (L1 error) of the "emulated" solution to the reference "solved" one.

As a result, the emulator pretrained (offline) in the previous section captures well the main flow pattern in the ELA-varying and A/c-varying experiments of Aletsch Glacier when ice flow parameters are fixed (Fig. 10) with an L1 error of ∼5 m/y (Fig. 9), which is relatively small compared to the velocity scale (0-200 m/y). This shows that the shape of the Aletsch Glacier is relatively well represented in the glacier catalogue (Fig. 17). Therefore, the emulator has acquired the right knowledge to predict a solution close to the "solved" one. Most of the error is concentrated on the glacier tongue – the emulator overestimates the ice flow compared to the reference "solved" solution (Fig. 10). This overestimation leads to a cumulative error: because the "emulated" flow being faster, the glacier naturally gets less mass, leading to underestimated ice volume (Fig. 9). In contrast, the offline trained emulator performs poorly with the Valais Glacier (Figs. 11 and 12). This is likely due to the fact that the glaciers used in this experiment go well beyond the

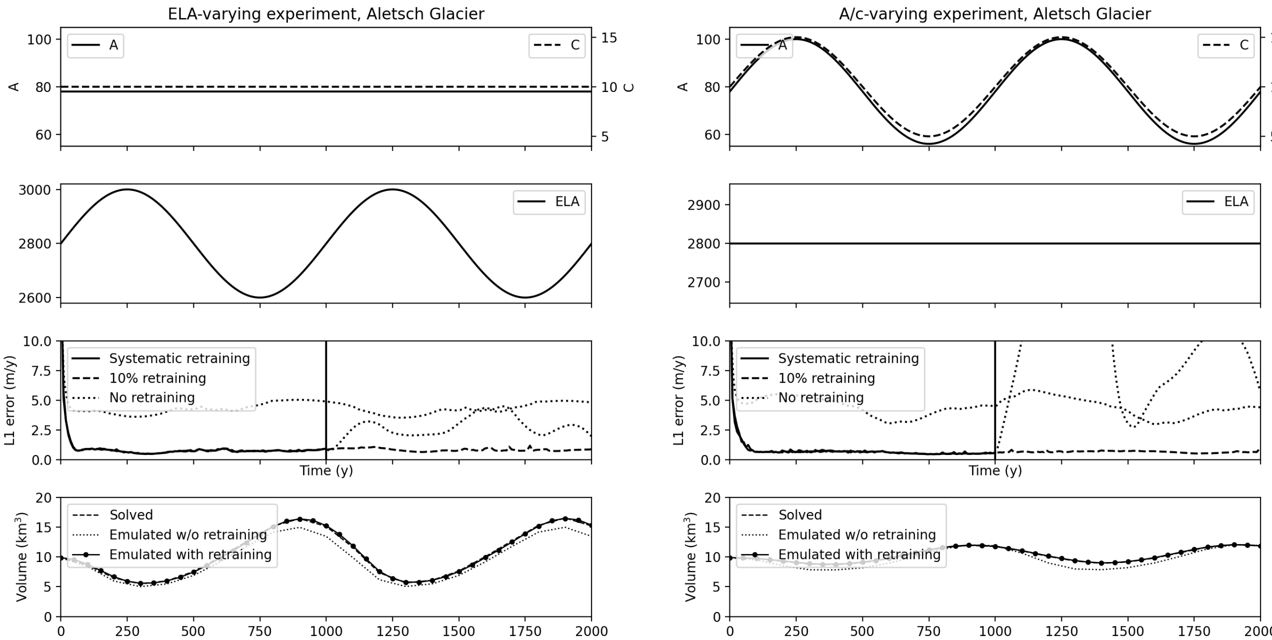

Fig. 9. Transient results of the ELA-varying (left panels) and A/c-varying (right panels) transient modelling experiments for Aletsch Glacier. The panels indicate the time evolution of input parameters (ice flow parameters and ELA), the resulting ice flow L1 error between all "emulated" solutions (with and without retraining) and the "solved" one, and the output ice volume obtained with the three modelling methods ("solved", "emulated" with and without retraining).

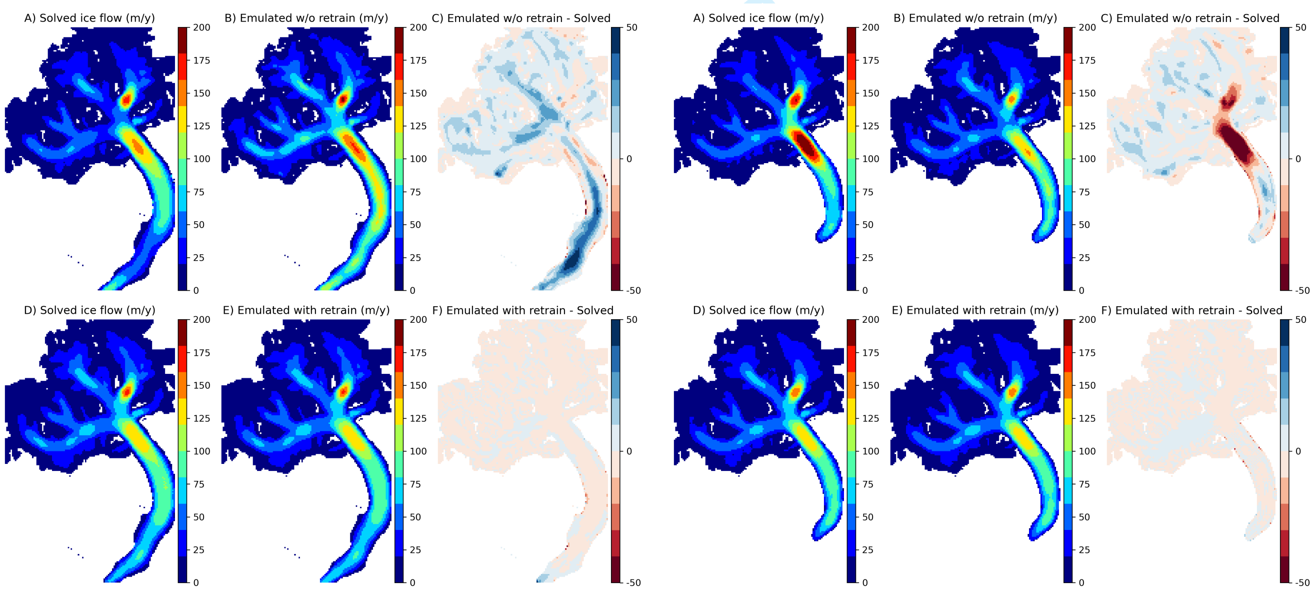

Fig. 10. Results of the ELA-varying (left panels) and A/c-varying (right panels) transient modelling experiments for Aletsch Glacier. The panel shows the surface ice flow magnitude at its maximum state (after 800 years): the "solved" solution (A), the "emulated" solution without (B) and with retraining (D), as well as the difference between the "emulated" and "solved" solutions (E and F).

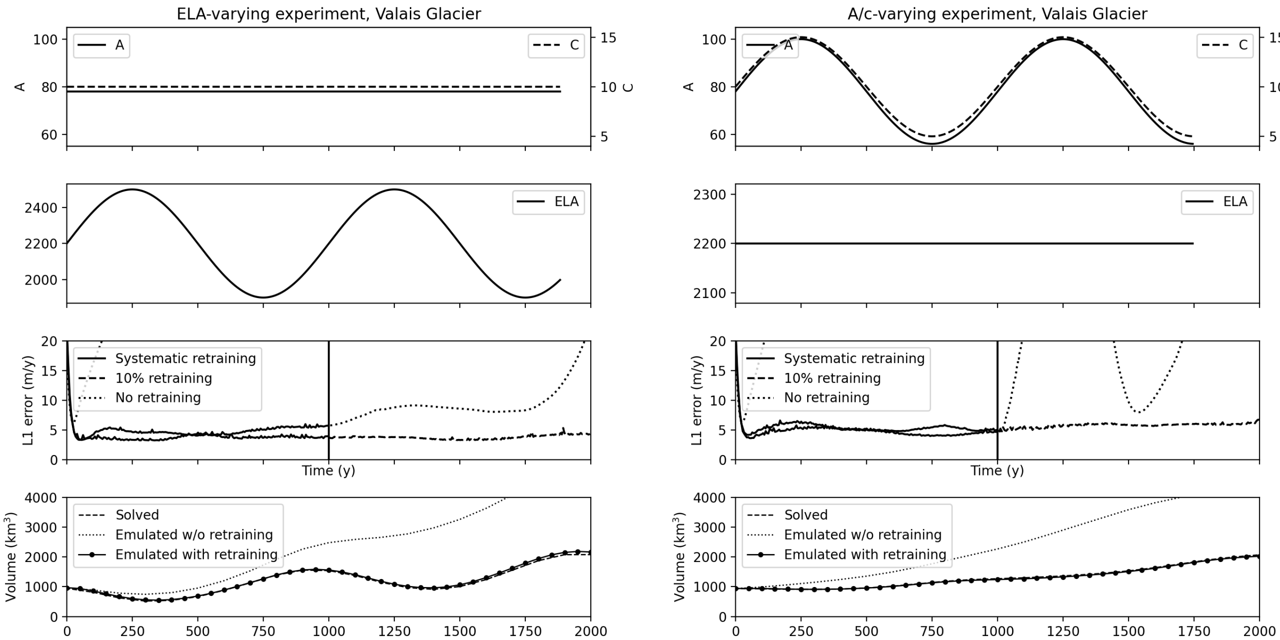

Fig. 11. Transient results of the ELA-varying (left panels) and A/c-varying (right panels) transient modelling experiments for Valais Glacier. This is similar to the caption of Figure 9.

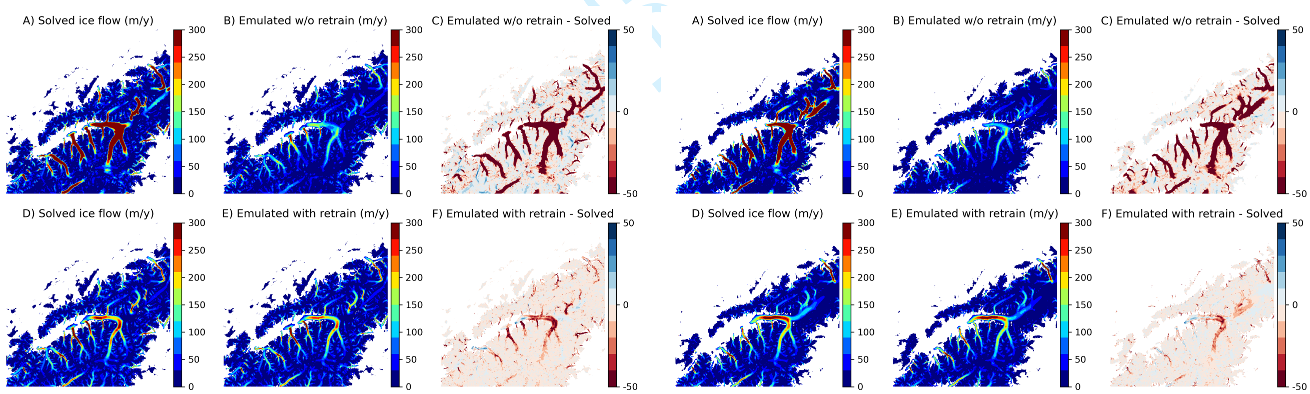

Fig. 12. Results of the ELA-varying (left panels) and A/c-varying (right panels) transient modelling experiments for Valais Glacier. Similar to the caption of Figure 10.

glaciers in the catalogue (Fig. 17) in terms of shape, size, and ice flow behaviour.

In contrast, our results reveal that adaptive online retraining of the emulator shows largely improved accuracy with respect to the "solved" reference solution, the two being mostly not distinguishable (Fig. 12). Indeed, retraining damps the L1 error to small values: below 1 m/y and 5 m/y in the Aletsch and the Valais Glacier experiments, respectively (Fig. 9 and 11) in the first 1000 years when retraining is applied to each time step. The spatial pattern of the the error reveals minor discrepancies, mostly in the trunk of Valais Glacier only. As a result of the high accuracy of the emulator, the modelled volumes agree very well with the "solved" solution when retraining is used.

As systematic online retraining during the first 1000 years is a costly task (next section), we analyse the effect of releasing the retraining or keeping only a light retraining to assess the capability of the emulator to retain the ice flow solutions accurately (Fig. 9 and 11). As a result, switching off the retraining after 1000 years of simulation and repeating the experiments with the same forcing for another 1000 years reveal different outcomes. Indeed, the emulator "retains" some of the relevant training in ELA-varying experiments, but deteriorates very quickly in the A/c-varying experiments, leading to notable biases in ice volume (Figs. 9 and 11). In contrast, the emulator remains nearly as accurate as in the first phase when lightly retrained in the second phase (i.e., at a frequency of 1 training step each 10 iterations, i.e. about every 1 model year). This means that the emulator has mostly retained the geometry-ice flow relationship during the first pass and that the accuracy can be maintained with a light computationally effective retraining provided a first initial intensive training.

An important parameter for online retraining is the learning rate. A too low parameter (gently learning) will result in inefficient learning and solution biases, while a too high parameter (aggressive learning) will result in erratic/non-smooth accuracy curve and deteriorated memory of the emulator (not shown). As a trade-off between the two cases, we found that a learning rate of 2×10^{-5} is optimal in all our experiments.

Computational performance

We now compare the computational performance of the 3 solutions: "solved", "emulated with offline retraining" and "emulated with online retraining" to lead the ELA and A/c-varying experiments presented in the previous section. Comparing the emulator and the solver is a challenge, as the first requires only one emulation, while the second may require several iterations per time step to converge. For this reason, we first discuss the costs associated with each individual step before analysing the overall costs.

Table 1 gathers together the computational times needed to achieve one step of i) solving, ii) emulating, and iii) retraining for modelling domains of various sizes, and on both CPU and GPU architectures of a same desktop computer (equipped with a 10-core Intel CPU i9-10900K and a 10'000 cores Nvidia GPU RTX 3090). As a result, the GPU (which has 1000 times more cores) systematically over-performs the CPU. While the CPU may be interesting for small-scale array domains, Table 1 shows that it is not a viable option to treat large-scale arrays. Therefore, we focus our performance analysis on the GPU only. We find that the emulation step is the most affordable task, followed by the solving step, which is slightly (about

[!ht]

Exp	Step	CPU	GPU
Aletsch	solver	125 ms	15 ms
244x179	emulator	39 ms	11 ms
	retrain	533 ms	29 ms
Valais	solver	1538 ms	51 ms
700x700	emulator	468 ms	38 ms
	retrain	5592 ms	110 ms
Entire Alps	solver	—	—
2400x4000	emulator	—	360 ms
	retrain	—	1465 ms

Table 1. Computational time required (in average) to perform one emulation, retraining, solving steps in modelling experiments for Aletsch, Valais, and the entire Alps. We use — when the computation was not possible, or prohibitively too expensive. The CPU (i9-10900K) has 10 3.70 GHz cores with 64 Gb RAM while the GPU (RTX 3090) has about 10'000 1.70 GHz cores with 24 Gb RAM.

30%) more expensive, and the retraining step, which is about 3 times more expensive than emulation regardless of the domain size. This can be explained as follows. The emulation step is inexpensive as it only requires a single pass of the CNN. On the other hand, the solving step consists of a forward evaluation of the system energy followed by the computation of the energy gradients and an update of the ice flow. Last, the retraining step is naturally expected to be more costly than the "emulation + solving", as it combines the tasks of the two: one CNN evaluation, one system energy evaluation, the computation of the two gradients and an update of the weights of the CNN.

Since a CNN is evaluated sequentially layer by layer, the emulation step is memory-effective. Therefore, emulation step can be performed on large arrays (i.e. we achieved 2400x4000 with our 24 Gb GPU, Table 1), the solving and retraining steps are more memory-demanding and therefore more limited by the GPU available memory. For example, none of the solving and retraining steps for the 2400x4000 domain was achievable with our GPU (we found that a maximum grid of about 2000x2000). Hopefully, this limitation can be overcome for the retraining (and not for the solving step, Table 1) by splitting the domain into smaller patches and sequentially retraining the emulator patch-wise.

As the other modules (ice thickness and mass balance updates) are computationally inexpensive compared to the ice flow model, the overall cost is mainly the number of time iterations times the costs of individual emulation or solver steps. Here, we analysed the costs associated with a single step. However, it is known that several steps of solving are usually required to reach convergence, and this number is usually case-dependent. Therefore, Table 1 shows that we must favour emulator steps over solver steps, and reduce as many retraining steps as possible. As a consequence, the best trade-off in terms of accuracy to computational performance is to apply online systematic retraining when modelling glacier conditions that were not seen previously by the emulator, or light retraining when that was the case. Indeed, the high cost of retraining can be mitigated by reducing its frequency. As a result, using a sparsely retrained emulator can maintain a high accuracy level at a price that is close to using the emulator only (e.g. if one used each 10 iterations, Figs. 9 and 11).

APPLICATIONS

In this section, we illustrate the potential of our physics-informed ice-flow emulator for glaciological applications.

Paleo glacier modelling in the European Alps

Modelling paleo-glacier evolution is an important tool for understanding the history of glaciations. However, the long time scales and the size of the domain may render this exercise computationally very demanding. For example, the 120 000-year-long simulation of alpine glacier evolution in the Alps of Jouvet et al. [under minor revision] at 2 km with the Parallel Ice Sheet Model [PISM, Khroulev and the PISM Authors, 2020] would take about one month of computational time on the 10 3.70 GHz cores CPU (i9-10900K). It is, therefore, prohibitively expensive to explore subkilometre resolutions that would be required to resolve the complex topography of the Alps in the highest reaches. Therefore, the ice flow emulator with online retraining is a promising approach to overcome the computational bottleneck, especially on GPU, which allows large array computations. Here, we test its capability to simulate the paleo evolution of glaciers in the entire European Alps in very high resolution (200 m) over 10’000 years encompassing the Last Glacial Maximum (LGM, about 24’000 years ago).

To this end, we took over the model setting of Jouvet et al. [under minor revision]. Initialising with ice-free conditions and today’s topography of the Alps as bedrock, IGM was forced with a coupled modelled paleoclimate data and PDD surface mass balance model [Hock, 1999] from 28’000 years BP to 18’000 years BP. As a result, the 200 m IGM simulation at 21’000 years BP shows highly detailed glacier extents

[!h]

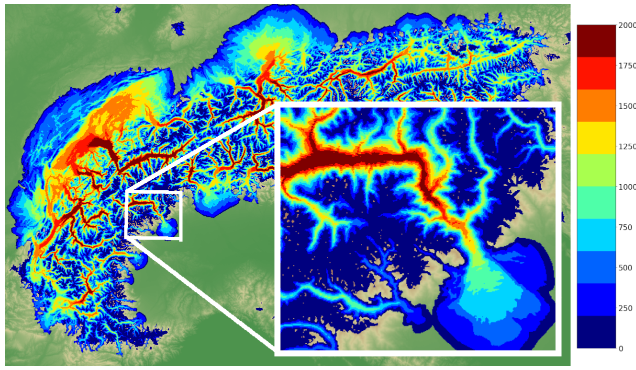

Fig. 13. Ice thickness of the alpine ice field obtained at 21'000 years BP modelled with IGM at 200 meters of resolution.

resolving small valleys and Nunataks (Fig. 13), and took about 2 days of computations on a ∼10'000-core RTX 3090 1.70 Ghz GPU. Here, the GPU has 24 GB memory, which is key to treating very large arrays; The horizontal grid covers the entire Alps at 200 metres of resolution is 2400x4000. This exercise illustrates the capability of our approach to achieve very high resolutions at affordable computational costs. For comparison, PISM at a much lower resolution (2km resolution, 240x400) would take about the same time (about 2 days) to carry a similar simulation on a 10-core 3.70 GHz CPU. Of course, this comparison must be tempered by the fact that IGM does not include all the many physical components of PISM, especially the thermodynamics of ice, which is known to add substantial computational time.

Ice flow model inversion/data assimilation

Inverse modelling is an essential step to initialise present-day glacier models, i.e., to seek for unknown variables (such as ice thickness and/or ice flow parameters) such that the model matches at best observations (surface ice flow velocities or pointwise ice thickness profiles). Substituting the ice flow equations with a CNN emulator allows to solve the inverse model (or the underlying optimisation problem) very efficiently by utilising automatic differentiation and stochastic gradient methods [Jouvet, 2023]. Therefore, the CNN emulator trained by physics-informed deep learning can also be used in a similar way. Most importantly, one can now simultaneously optimise the CNN parameters to fit the ice physics by minimising the system energy and the CNN inputs to match observations by minimising the misfit to the data. The coupled optimisation allows to perform the inversion with an accurate and customised-to-the-glacier CNN at the same time.

[!h]

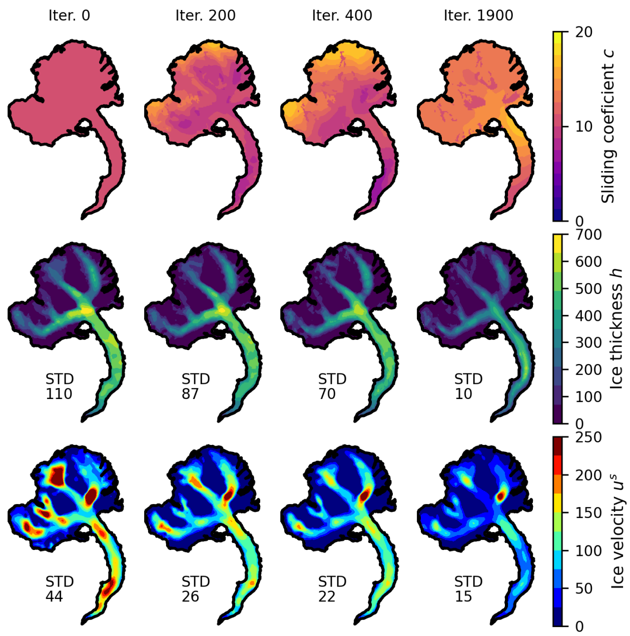

Fig. 14. Evolution of the sliding distribution c (unit: km MPa^{-3} a^{-1}), the ice thickness distribution h (unit: m), as well as resulting surface ice flow velocity field $\mathbf{u}^s$ (unit: m y^{-1}) through the iterations of the optimisation problem for Aletsch glacier. The STandard Deviation (STD) between the modeled and observed fields is reported at each step.

As an illustration, we solve the inversion problem for Aletsch Glacier proposed by Jouvet [2023] with this new strategy. Given present-day pointwise ice thickness measurements and surface ice velocity measurements, we use the CNN trained offline over the glacier catalogue, and seek alternatively for the CNN weights λ, the ice thickness distribution h and the distributed sliding parameter c, such that both the system energy (Eq. (19)) and the mismatch between the observed and modelled quantities (Eq. (5) in Jouvet [2023]) are minimised. Note that the regularisation terms for h and c are added to enforce smoothness and ensure a unique solution. As a result, Fig. 14 shows the convergence of the fields towards an optimal state and the reduction of the corresponding misfit values in terms of STandard Deviations (STD). Here, the quality of data assimilation is comparable to that obtained by Jouvet [2023]. However, the simultaneous emulator training/optimisation has a major benefit with respect to the former method (based on offline training): the online retraining permits to account for spatial variations of the sliding coefficient (Fig. 14, top-right panel) and makes the emulator nearly as accurate as the solver (Fig. 15). In contrast, the former emulator, which met only the glacier catalogue and spatially constant sliding coefficient at training, suffers from larger biases as observed in the previous section between offline and online training emulation results.

[!h]

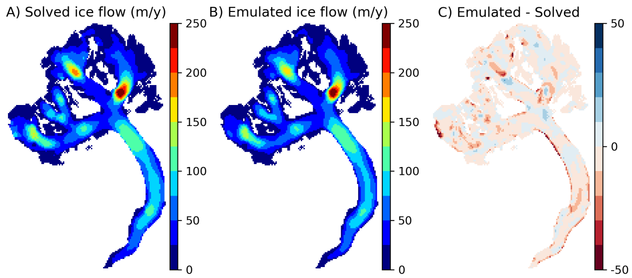

Fig. 15. Surface ice flow field of Aletsch Glacier with the parameters found after performing the simultaneous inversion and emulator training: A) using the solver B) using the retrained emulator. Panel C) shows the spatial difference between the two.

Ice shelf

Ice shelves behave very differently to mountain glacier ice flow as modelled in the two previous applications. Indeed, they can be very fast due to the absence of friction under floating ice, and are therefore dominated by basal sliding. By contrast, friction under grounded glaciers usually induces an important vertical shearing component. Yet, modelling accurately the dynamics of ice shelves is essential to predict the evolution of the Antarctic ice sheet under climate change and the resulting sea level rise [Seroussi et al., 2020]. Here we demonstrate that IGM equipped with the new physics-informed deep-learning emulator has an important potential for modelling ice sheet/shelf systems by performing a simple experiment inspired from the Marine Ice Sheet Model Inter-comparison Project [MISMIP Pattyn et al., 2012]. The goal here is not to run all exercise simulations, but only to compute the ice dynamics associated with one state to prove the capacity of the emulator too handle sliding-dominant ice flow of ice shelves.

For that purpose, we consider an idealized ice sheet-shelf geometry lying on a ramp of constant slope in the x-direction over a distance of $L_x = 1100$ km (Fig. 16). All geometrical variables are constant in the y-direction to mimic the 2D MISMIP experiment 1 [Pattyn et al., 2012]. In that configuration, we distinguish the ice sheet ($x < x_{GL}$) and the ice shelf ($x > x_{GL}$) from the the grounding location $x_{GL} \sim 966.5$ km (Fig. 16). The lower surface elevation l is either the bedrock when the ice is grounded or determined by Archimedes's principle when the ice is floating: $l = \max\{b, -(\rho_i/\rho_w)h\}$, where $\rho_i = 910$ kg m^{-3} and $\rho_w = 1000$ kg m^{-3} denote the densities of ice and water, respectively. Here, we use of the following parameters: $A = 146.5$ MPa^{-3} a^{-1}, $m = 1/3$, $c = 71.2$ km MPa^{-3} a^{-1} where the ice is grounded and $c^{-1} = 0$ km MPa^{-3} a^{-1} where the ice is floating (no friction). In addition, we use the "Shallow Shelf

[!h]

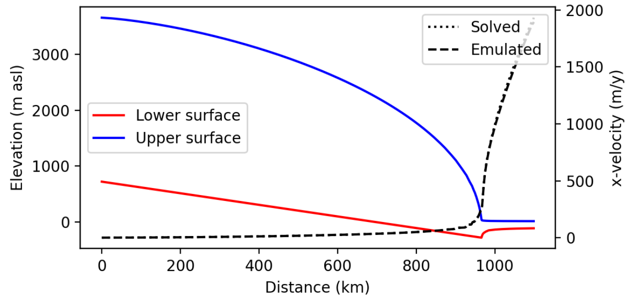

Fig. 16. MISMIP-inspired ice geometry of the ice shelf experiment along the x-axis, and resulting ice flow velocities modelled from the solver and the emulator with custom training on the specific geometry.

Approximation" (SSA) model [Morland, 1987] instead of the FOA by simply setting a single layer in the vertical discretization (Fig. 2, right panel), which is equivalent to assuming vertically-constant ice flow velocities. Lastly, the function $\mathcal{J}$ defined by (14) is augmented with an additional term to account for balance stress conditions between ice and water columns at the Calving Front (CF) on the extreme right of the modelled domain (Fig. 16):

$$-\int_{CF} \frac{1}{2}\left(1 - \frac{\rho_i}{\rho_w}\right) \rho_i g h^2 v \cdot \mathbf{n}, \qquad (22)$$

where $\mathbf{n}$ is an outer normal vector along CF [Schoof, 2006]. The above condition (22) was implemented along the other terms of the system energy, and a 2D field was added to the emulator inputs (Eq. (18)) to control this boundary condition.

As a result, we find that after training the emulator on the specific geometry, the "Solved" and "Emulated" ice flow fields along the x-axis are nearly identical (Fig. 16). This experiment demonstrates that the approach of the paper is not limited to grounded glacier flow, but is capable to handle sliding-dominant flow of ice shelves. Similarly to the paleo modelling application, using a deep-learning emulator to model large scale Antarctica or Greenland ice sheets in high-resolution on GPU opens promising perspectives to overcome the current computational bottleneck of traditional models.

DISCUSSION AND CONCLUSIONS

In this paper, we have introduced a solver and a physics-informed deep learning emulator for modelling high-order ice flow on a uniform grid that are designed to run efficiently on GPU. The solver relies on a stochastic gradient method and automatic differentiation tools to efficiently minimise the energy associated with the underlying ice-flow equations, similarly to Ritz-Galerkin methods in the finite element framework. On the other hand, the emulator relies on a CNN, which is trained to minimise the same energy using similar optimisers. Therefore, our method (which belongs to the category of Deep-Ritz) can be seen as a fusion of finite element and deep learning approaches. Here, our approximation space for the ice flow is spanned by the training parameters of our CNN instead of being spanned by finite element basis functions. As a result, we have shown that our emulator can reproduce the solutions of the solver fairly well when trained over a generic catalogue of glacier shapes provided a test glacier characteristics similar to the ones of the catalogue, and with very high fidelity levels when trained specifically on the test glacier. Unlike the former emulator introduced by Jouvet et al. [2022], the new emulator does not require any data from an external ice flow model, as it enforces the ice flow physics directly in learning. Here, we used a glacier catalogue to pre-train the emulator for convenience. However, adaptive online training within the time-stepping of a glacier evolution model does not require any data and has proven to significantly improve the emulator accuracy. This strategy makes the new emulator generic, as it allows exploration of any parameters, types of ice flow, spatial resolutions, and glacier shapes, while the validity of the former emulator could not be ensured beyond the "hull" defined by the data and its associated resolution used for training. In addition, CNN training is therefore significantly easier and cheaper as no data is required. Last, our new emulator models the full 3D ice flow field (instead of the vertically average horizontal speeds with the former version), which can be advantageous for some applications (e.g., Lagrangian 3D particle tracking).

The computational benefits of using a CNN emulator instead of a solver given by Jouvet et al. [2022] remain unchanged. Indeed, one CNN forward evaluation can be done very efficiently, especially on GPU. In contrast, the solving and training steps are computationally more expensive (by a factor of 3 in our experiments). Therefore, to obtain the best computational performances, we mitigate the amount of training by doing some preliminary custom training, or limiting the frequency of retraining – a strategy that depends on the type of application. Hopefully, the memory capability of the CNN revealed in our experiments allows us to reduce the training costs for a given application. For instance, we found that an emulator pre-trained (offline) on a glacier catalogue and parameter set in a preliminary phase may be sufficient for modelling glaciers that are similar to the ones in the catalogue without further retraining. Should the pre-trained emulator show too high biases, a light cost-effective online retraining will be sufficient to maintain accuracy, as the CNN conserves most of the previously learnt solutions. Therefore, custom training costs can be strongly limited in some modelling applications that meet several times similar glacier configurations (e.g., in paleo glacier modelling with repeated glacial cycle, or in parameter sensitivity analysis), yielding low overall computational costs.

There are a number of aspects that may be improved in the method presented in this paper. First, we used here the simplest finite-difference scheme to discretise the spatial derivative in the strain rate on a staggered grid for simplicity. A more elaborated finite-element-like discretization is expected to yield a more accurate solution, possibly slightly increasing the training costs but without affecting the emulation costs. Second, we used here the Adam optimiser as it proved to be robust and simple to implement, however, other optimisers may improve the convergence. For example, the (deterministic) L-BFGS-B optimiser has proven to be efficient at fine-optimising physics informed neural networks after an initial coarse pass with Adam to avoid local minima [Taylor et al., 2022]. Lastly, we quantified *a posteriori* the error between the emulated and solved solutions. The derivation of error estimates for neural network approximation [similarly to traditional FEM, Ern and Guermond, 2004] is active domain of research [e.g. Minakowski and Richter, 2023], giving the hope that the error can be estimated to design optimal retraining strategies (in terms of quantifiable accuracy versus additional investment in training cost).

Our modelling experiments have shown that the new emulator embedded in a glacier evolution model can handle very efficiently large-scale and/or high-resolution domain arrays and/or very long time scales. Therefore, our method has a high potential for paleo-glacier simulations. Additionally, we found that the emulator is suitable for both inverse and forward modelling. Therefore, the method can be very beneficial to assimilate data and run prognostic models of present-day glaciers on a global scale. Lastly, we have shown that our approach can be extended to fast-flowing ice as found in tidewater glaciers, opening promising perspectives for modelling the Antarctica and Greenland ice sheets in high spatial resolution. The code to solve, train and evaluate the emulator, as well run emulator-based glacier evolution simulations is open-source, relatively simple and publicly available with the "Instructed Glacier Model" (IGM, `https://github.com/jouvetg/igm`).

AUTHOR CONTRIBUTIONS

GJ conceived the study, wrote the code, performed the simulations, and wrote the article. GC developed simultaneously a similar approach, provided valuable feedback on the method and the results, and helped to improve the manuscript.

REFERENCES

M. Abadi, A. Agarwal, P. Barham, E. Brevdo, Z. Chen, C. Citro, G. S. Corrado, A. Davis, J. Dean, M. Devin, S. Ghemawat, I. Goodfellow, A. Harp, G. Irving, M. Isard, Y. Jia, R. Jozefowicz, L. Kaiser, M. Kudlur, J. Levenberg, D. Mané, R. Monga, S. Moore, D. Murray, C. Olah, M. Schuster, J. Shlens, B. Steiner, I. Sutskever, K. Talwar, P. Tucker, V. Vanhoucke, V. Vasudevan, F. Viégas, O. Vinyals, P. Warden, M. Wattenberg, M. Wicke, Y. Yu, and X. Zheng. TensorFlow: Large-scale machine learning on heterogeneous systems, 2015. URL `https://www.tensorflow.org/`. Software available from tensorflow.org.

R. Adams and J. Fournier. *Sobolev Spaces*. Pure and Applied Mathematics. Elsevier Science, 2003. ISBN 9780080541297. URL `https://books.google.ch/books?id=R5A65Koh-EoC`.

H. Blatter. Velocity and stress fields in grounded glaciers: a simple algorithm for including deviatoric stress gradients. *Journal of Glaciology*, 41(138):333–344, 1995.

C. F. Brædstrup, A. Damsgaard, and D. L. Egholm. Ice-sheet modelling accelerated by graphics cards. *Computers & Geosciences*, 72:210–220, 2014.

D. Brinkerhoff, A. Aschwanden, and M. Fahnestock. Constraining subglacial processes from surface velocity observations using surrogate-based bayesian inference. *Journal of Glaciology*, pages 1–19, 2021. doi: 10.1017/jog.2020.112.

E. Bueler and J. Brown. Shallow shelf approximation as a “sliding law" in a thermomechanically coupled ice sheet model. *Journal of Geophysical Research – Earth Surface*, 114(F3), 2009. doi: 10.1029/2008JF001179.

F. Chollet et al. Keras. `https://github.com/fchollet/keras`, 2015.

J. Colinge and J. Rappaz. A strongly nonlinear problem arising in glaciology. *M2AN Math. Model. Numer. Anal.*, 33(2):395–406, 1999. ISSN 0764-583X.

G. Cordonnier, G. Jouvet, et al. Forming terrains by glacial erosion. *Conditionally accepted to Siggraph 2023 (minor revision)*, 2023.

T. Cui, Z. Wang, and Z. Zhang. A variational neural network approach for glacier modelling with nonlinear rheology. *arXiv preprint arXiv:2209.02088*, 2022.

A. Ern and J.-L. Guermond. *Theory and practice of finite elements*, volume 159. Springer, 2004.

V. Girault and P. Raviart. *Finite Element Methods for Navier-Stokes Equations: Theory and Algorithms*. Springer Series in Computational Mathematics, 1986.

J. W. Glen. Rate of Flow of Polycrystalline Ice. *Nature*, 172:721–722, 1953. doi: 10.1038/172721a0.

M. Grab. Swiss glacier thickness – release 2020, 2020.

R. Greve and H. Blatter. *Dynamics of Ice Sheets and Glaciers*. Springer Verlag, 2009.

R. Hock. A distributed temperature-index ice- and snowmelt model including potential direct solar radiation. *Journal of Glaciology*, 45(149):101–111, 1999.

K. Hutter. *Theoretical Glaciology*. Reidel, 1983.

G. Jouvet. Mechanical error estimators for shallow ice flow models. *Journal of Fluid Mechanics*, 807:40–61, 2016.

G. Jouvet. Inversion of a stokes glacier flow model emulated by deep learning. *Journal of Glaciology*, 69(273):13–26, 2023.

G. Jouvet and M. Huss. Future retreat of great aletsch glacier. *Journal of Glaciology*, 65(253):869–872, 2019.

G. Jouvet, J. Seguinot, S. Ivy-Ochs, and M. Funk. Modelling the diversion of erratic boulders by the valais glacier during the last glacial maximum. *Journal of Glaciology*, 63(239):487–498, 2017.

G. Jouvet, G. Cordonnier, B. Kim, M. Lüthi, A. Vieli, and A. Aschwanden. Deep learning speeds up ice flow modelling by several orders of magnitude. *Journal of Glaciology*, 68(270):651–664, 2022.

G. Jouvet, D. Cohen, E. Russo, J. Buzan, C. Raible, U. Hischer, W. Haeberli, S. Kamleitner, S. Ivy-Ochs, M. Imhof, J. Becker, and A. Landgraf. Coupled climate-glacier modelling of the last glaciation in the alps. *Journal of Glaciology (Under minor revision)*, under minor revision.

E. Kharazmi, Z. Zhang, and G. E. Karniadakis. Variational physics-informed neural networks for solving partial differential equations. *arXiv preprint arXiv:1912.00873*, 2019.

C. Khroulev and the PISM Authors. PISM, a Parallel Ice Sheet Model v1.2: User's Manual. 2020. URL `www.pism-docs.org`.

D. P. Kingma and J. Ba. Adam: A method for stochastic optimization. *arXiv preprint arXiv:1412.6980*, 2014.

Y. LeCun, Y. Bengio, and G. Hinton. Deep learning. *nature*, 521(7553):436–444, 2015.

J. Long, E. Shelhamer, and T. Darrell. Fully convolutional networks for semantic segmentation. In *Proceedings of the IEEE conference on computer vision and pattern recognition*, pages 3431–3440, 2015.

A. L. Maas, A. Y. Hannun, and A. Y. Ng. Rectifier nonlinearities improve neural network acoustic models. In *Proc. icml*, volume 30, page 3, 2013.

S. Markidis. The old and the new: Can physics-informed deep-learning replace traditional linear solvers? *Frontiers in big Data*, page 92, 2021.

F. Maussion, A. Butenko, N. Champollion, M. Dusch, J. Eis, K. Fourteau, P. Gregor, A. H. Jarosch, J. M. Landmann, F. Oesterle, et al. The open global glacier model (oggm) v1. 1. *Geoscientific Model Development*, 12(3):909–931, 2019.

P. Minakowski and T. Richter. A priori and a posteriori error estimates for the deep ritz method applied to the laplace and stokes problem. *Journal of Computational and Applied Mathematics*, 421:114845, 2023.

L. Morland. Unconfined ice-shelf flow. In C. Veen and J. Oerlemans, editors, *Dynamics of the West Antarctic Ice Sheet*, volume 4 of *Glaciology and Quaternary Geology*, pages 99–116. Springer Netherlands, 1987. ISBN 978-94-010-8171-9. doi: 10.1007/978-94-009-3745-16. URL `http://dx.doi.org/10.1007/978-94-009-3745-16`.

W. S. B. Paterson. *The Physics of Glaciers*. Pergamon, New York, third edition, 1994.

F. Pattyn and . others. Benchmark experiments for higher-order and full-Stokes ice sheet models (ISMIP-HOM). *The Cryosphere*, 2(2):95–108, 2008. doi: 10.5194/tc-2-95-2008. URL `http://www.the-cryosphere.net/2/95/2008/`.

F. Pattyn, C. Schoof, L. Perichon, R. C. A. Hindmarsh, E. Bueler, B. de Fleurian, G. Durand, O. Gagliardini, R. Gladstone, D. Goldberg, G. H. Gudmundsson, P. Huybrechts, V. Lee, F. M. Nick, A. J. Payne, D. Pollard, O. Rybak, F. Saito, and A. Vieli. Results of the marine ice sheet model intercomparison project, mismip. *The Cryosphere*, 6(3):573–588, 2012. doi: 10.5194/tc-6-573-2012. URL `https://tc.copernicus.org/articles/6/573/2012/`.

M. Raissi, P. Perdikaris, and G. E. Karniadakis. Physics-informed neural networks: A deep learning framework for solving forward and inverse problems involving nonlinear partial differential equations. *Journal of Computational physics*, 378:686–707, 2019.

L. Räss, A. Licul, F. Herman, Y. Y. Podladchikov, and J. Suckale. Modelling thermomechanical ice deformation using an implicit pseudo-transient method (FastICE v1. 0) based on graphical processing units (GPUs). *Geoscientific Model Development*, 13(3):955–976, 2020.

B. Riel and B. Minchew. High-dimensional flow law parameter calibration and uncertainty quantification over antarctic ice shelves: a variational bayesian approach using deep learning. *Authorea Preprints*, 2022.

B. Riel, B. Minchew, and T. Bischoff. Data-driven inference of the mechanics of slip along glacier beds using physics-informed neural networks: Case study on rutford ice stream, antarctica. *Journal of Advances in Modeling Earth Systems*, 13(11):e2021MS002621, 2021.

C. Schoof. Variational methods for glacier flow over plastic till. *J. Fluid Mech.*, 555:299–320, 2006.

C. Schoof and I. Hewitt. Ice-sheet dynamics. *Annual Review of Fluid Mechanics*, 45(1):217–239, 2013. doi: 10.1146/annurev-fluid-011212-140632.

H. Seroussi, S. Nowicki, A. J. Payne, H. Goelzer, W. H. Lipscomb, A. Abe-Ouchi, C. Agosta, T. Albrecht, X. Asay-Davis, A. Barthel, et al. Ismip6 antarctica: a multi-model ensemble of the antarctic ice sheet evolution over the 21st century. *The Cryosphere*, 14(9):3033–3070, 2020.

J. Taylor, W. Wang, B. Bala, and T. Bednarz. Optimizing the optimizer for data driven deep neural networks and physics informed neural networks, 2022.

B. Yu et al. The deep ritz method: a deep learning-based numerical algorithm for solving variational problems. *Communications in Mathematics and Statistics*, 6(1):1–12, 2018.

APPENDIX A: GLACIER CATALOGUE

To generate glacier shape inputs in an offline training process of the CNN, we use a glacier catalogue of 36 mountain glaciers at 8 different times and 100 m resolution (covering advancing and retreating stages) obtained by Jouvet et al. [2022] by glacier evolution simulations (Fig. 17). Further details about the construction of this catalogue are given in Appendix C of Jouvet et al. [2022]. The catalogue consists of a heterogeneous dataset with a large variety of possible glacier shapes (large/narrow, thin/thick, flat/steep, long/small, straight/curved glaciers, . . .).

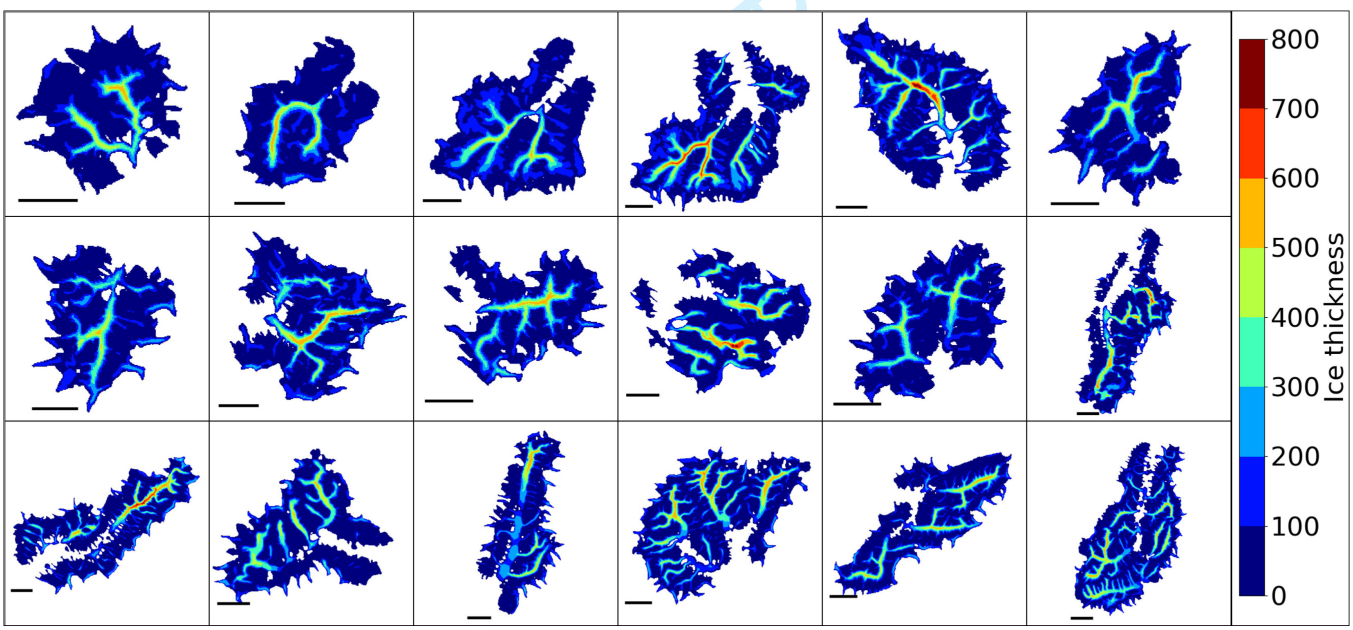

Fig. 17. Ice thickness at their maximum extent of half of the glacier catalogue (18 of the 36). Each glacier shape is a snapshot of a simulation initialised with ice-free conditions, and forced with a surface mass balance that permits building and retreat successive phases over a total of 200 years. The horizontal bar represents 5 km to give the scale of each glacier.